Journal of Materials Chemistry A

PAPER

View Article Online
View Journal | View Issue

Cite this: J. Mater. Chem. A, 2015, 3, 8643

Construction of a 3D-rGO network-wrapping architecture in a $Yb_yCo_4Sb_{12}$/rGO composite for enhancing the thermoelectric performance†

Peng-an Zong,[ae] Xihong Chen,[b] Yanwu Zhu,[c] Ziwei Liu,[d] Yi Zeng[d] and Lidong Chen*[af]

Received 2nd March 2015
Accepted 11th March 2015

DOI: 10.1039/c5ta01594d

www.rsc.org/MaterialsA

Nanostructures and nano-composites have been shown to be effective in depressing the lattice thermal conductivity and improving the performance of thermoelectric materials. However, *ZT* enhancement by nano-particle dispersion is limited only to a restricted level due to the difficulty in increasing the particle contents while maintaining a uniform and narrow size distribution. In the present work, $Yb_yCo_4Sb_{12}$-based nano-composites with reduced graphene oxide (rGO) layers of several nanometers intercalated on the grain boundary matrix forming a 3D network have been prepared through a simple *in situ* reduction approach using graphene oxide (GO) as the precursor. The 3D-rGO network wrapping architecture dramatically reduced the lattice thermal conductivity due to enhanced interparticle and intraparticle phonon scattering effects, and simultaneously enhanced the Seebeck coefficient due to the energy filtering effect of the grain boundary semiconductive rGO layer with nanometer thickness. The maximum *ZT* value of 1.51 was achieved for the $Yb_{0.27}Co_4Sb_{12}$/rGO (0.72 vol%) composite at 850 K, outperforming all single-filled skutterudites and their nanocomposites ever reported.

1. Introduction

Thermoelectric effects enable direct conversion between thermal energy and electricity providing a promising solution for global sustainable energy. The efficiency of a thermoelectric device is basically determined by a dimensionless figure of merit (ZT) of thermoelectric materials, quantified by $ZT = (S^2\sigma T)/\kappa$, ($\sigma$, S, T and κ are the Seebeck coefficient, electrical conductivity, absolute temperature and thermal conductivity, respectively). The thermal conductivity κ is composed of two components: (i) the electron part κ_E, contributed from heat transportation by carriers; (ii) the phonon part κ_L, contributed from heat transportation by phonons travelling through the lattice.[1,2] In the past decade, effective strategies have been used to tune the thermal and electrical transport,[3–8] and many novel thermoelectric materials with enhanced *ZT*s have been reported.[9–16] Among them, $CoSb_3$-based filled skutterudites (SKD) are one of the most promising materials for power generation applications in the mediate temperature range. In $CoSb_3$-based skutterudites with cage structure, filling one or multiple kinds of guest atoms (alkali metals, alkaline earth, rare earth, and some other ions) into the intrinsic Sb-icosahedron cage has been shown to be effective in suppressing the lattice thermal conductivity with a minimized influence on electrical transport. Typically, the maximum *ZT* value of over 1.7 has been achieved for multiple-filled skutterudites, in which two or three kinds of elements with different resonant frequencies were filled into the Sb-icosahedron cage to scatter phonons in a broad range of frequencies, with optimized filling contents for optimizing charge concentration.[3]

Compared to multiple-filled skutterudites, single-filled skutterudites have also attracted great attention for mass production for industrial applications, because their simple composition leads to better controllability of the process and potential for scaling-up and cost-down in industrial fabrication. Further reducing the lattice thermal conductivity is the most challenging but most effective for increasing the *ZT* values of single-filled skutterudites. Constructing a nano-structure or

[a]State Key Laboratory of High Performance Ceramics and Superfine Microstructure, Shanghai Institute of Ceramics, Chinese Academy of Sciences, Shanghai 200050, China. E-mail: chenlidong@mail.sic.ac.cn; zongpengan@student.sic.ac.cn; Fax: +86 21 52413122; Tel: +86 21 52414804

[b]CAS Key Laboratory of Materials for Energy Conversion, Shanghai Institute of Ceramics, Chinese Academy of Sciences, Shanghai 200050, China. E-mail: xhchen@mail.sic.ac.cn; Fax: +86 21 52413122; Tel: +86 21 52412520

[c]Department of Materials Science and Engineering, University of Science and Technology of China & Collaborative Innovation Center of Chemistry for Energy Materials (2011-iChEM), Hefei 230026, China. E-mail: zhuyanwu@ustc.edu.cn; Fax: +86 551 63601696; Tel: +86 551 6360767

[d]Analysis and Testing Center for Inorganic Materials, Shanghai Institute of Ceramics, Chinese Academy of Sciences, Shanghai 200050, China. E-mail: zengyi@mail.sic.ac.cn; ziweiliu@mail.sic.ac.cn; Fax: +86 21 52413903; Tel: +86 21 52413108

[e]University of Chinese Academy of Sciences, Beijing 100049, China

[f]Shanghai Institute of Materials Genome, Shanghai 200444, China

† Electronic supplementary information (ESI) available: SEM images of the 1.8 vol% 3D-rGO sample and 1.8 vol% particle dispersion sample respectively; TEM images of SKD/*y* vol% 3D-rGO samples (y = 1.8 and 3.6); and thermoelectric properties of SKD/*y* vol% particle dispersion samples (y = 0, 0.72, 1.8, and 3.6). See DOI: 10.1039/c5ta01594d

nano-composite is one of the most commonly used strategies for strengthening the phonon scattering.[2,11–16] So far, lots of skutterudite-based or filled skutterudite-based nanocomposites have been synthesized by dispersing different nano-particles, such as $CoSb_3/C_{60}$ (ref. 11) and $CoSb_3/ZrO_2$ (ref. 12) fabricated by mechanical mixing, $Ba_{0.22}Co_4Sb_{12}/TiO_2$ (ref. 13) by solution dispersion, and $Yb_xCo_4Sb_{12}/Yb_2O_3$,[14] $Yb_xCo_4Sb_{12}/Sb$[15] and $Yb_xCo_4Sb_{12}/GaSb$[16] by *in situ* reactions. Particularly, for the typical n-type filled skutterudite $Yb_xCo_4Sb_{12}$, which is one of the candidates for device applications, ZT_{max} values have been continuously enhanced by dispersing different nanoparticles from less than 1.2 (pure $Yb_xCo_4Sb_{12}$) to ~1.3 ($Yb_xCo_4Sb_{12}/Yb_2O_3$ (ref. 14)) and ~1.4 ($Yb_xCo_4Sb_{12}/GaSb$[16]). In these nano-particle dispersed systems, both the interfaces between the matrix and nano-particles and the nano-particles themselves act as the objectives to scatter phonons.[13–16] However, the depression of lattice thermal conductivity is still limited in such nanoparticle-dispersed systems, because the total amount of the nano-particles and the interfaces is limited to a relatively low level. Furthermore, the narrow size distribution of the nano-particles is difficult to obtain in bulk materials due to the agglomeration of nano-particles. Additionally, in oxide particle dispersed systems, electron scattering is also not negligible, which usually damages the electrical transport.

Recently, an ideal 3D network wrapping structure (or core–shell nanocomposites) has been proposed theoretically for strengthening the phonon scattering and holding the promise of *ZT*-plus.[17,18] According to this model, when the secondary phase disperses as a nanoscale shell layer on the grains of the matrix phase (core), the heat-carrying phonons would be much more effectively scattered than the particle dispersion system, because of the enhanced interparticle boundary scattering and intraparticle boundary scattering with an increased amount of interfaces. However, it is of great challenge to realize such a 3D network architecture in a bulk material. In addition, the 3D network wrapping nanocomposite demands more strict requirements on the electrical properties of the introduced wrapping phase so that it can scatter phonons but maintain good electron transport, because all the matrix grains would be wrapped by the dispersion phase. A high electrical conductivity with a suitable band gap matching with the matrix would be required because an extra potential at the boundaries would be expected to realize an energy-filtering effect[16] in such a 3D-wrapping structure. In order to satisfy these demands, we propose to use reduced graphene (rGO) as the wrapping phase because the band gap can be tuned by the reduction degree (the oxygen ratio in rGO).[19,20,21] We designed a $Yb_{0.27}Co_4Sb_{12}$-based composite with rGO nanolayers intercalated on the grain boundary forming a continuous 3D network. However, a big challenge arises in constructing such an rGO 3D-network architecture in SKD/rGO composites, because of the easy agglomeration[11–15] due to the poor dispersity of rGO. The graphene oxide (GO) is known to have better dispersity in appropriate agents or water solutions. In previous reports, $CoSb_3$/graphene[22] and PbTe/graphene[23] were synthesized by a wet chemical method, where the matrix-$CoSb_3$ and PbTe were fabricated by a solvothermal method and GO was concurrently reduced by $NaBH_4$. However, the graphene needs to become thinner and better its distribution to form an interconnected network to further depress the thermal conductivity, because the solvothermal method may lead to rapid agglomeration of graphene during the reduction of graphene, and the wet-chemically prepared matrix may restrict the optimization of the thermoelectric performance to some extent by deteriorating the electrical properties due to the relatively low purity of the matrix. We developed a simple *in situ* reduction approach to realize the 3D-rGO network wrapping structure using GO as the precursor. In this simple process, GO was dispersed into the solid-state-melting-method made $Yb_yCo_4Sb_{12}$ skutterudite (SKD) powder to fabricate the SKD/GO mixture, and then the powder mixture compact was densified using spark plasma sintering, whereby the GO was reduced to rGO. The rGO layers as thick as ~3–5 nm are homogeneously distributed on grain boundaries. The obtained SKD/rGO composite with a well-designed 3D network structure exhibited extremely low lattice thermal conductivity and a relatively high power factor (particularly high Seebeck coefficient) as compared with single-filled skutterudites and their composites. An enhancement of ~30% in the *ZT* value was achieved in the wide temperature range between 300 and 850 K with a maximum *ZT* value of 1.51 at 850 K.

2. Experimental section

2.1 Synthesis and sample preparation

$Yb_{0.27}Co_4Sb_{12}$ (SKD) powder was fabricated by a solid state melting method.[13] An improved Hummers method[21,24] was applied to synthesize GO from purified natural graphite (SP-1, Bay Carbon). Then 1.5 g fine SKD powder was dispersed in 200 ml deionized water, and 0.05 mg ml^{-1} GO water suspension solution was added dropwise, followed by ultrasonic treatment for 30 min. The mixture was then subjected to vacuum filtering, drying at 450 K in Ar-5 vol% H_2 gas flow for 4 h, and regrinding into fine powder. The SKD/GO mixture powder compacts were then sintered by spark plasma sintering in a graphite die in a vacuum at 900 K for 10 minutes under an axial pressure of 60

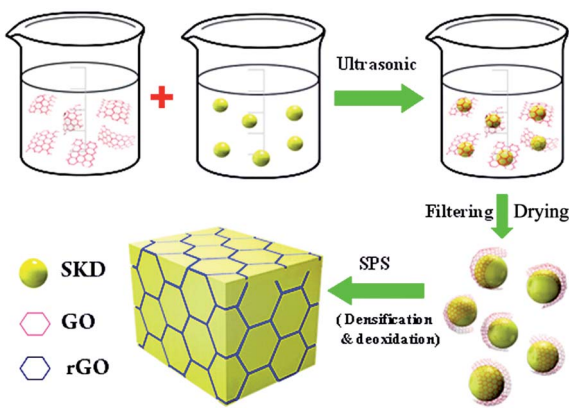

Fig. 1 Three-dimensional schematic showing the synthesis procedure of the 3D-rGO network wrapping architecture.

MPa, yielding fully densified bulk disk-shaped samples, containing various rGO contents ($y = 0$, 0.72, 1.8, and 3.6 vol%) in SKD. The synthesis process is schematically shown in Fig. 1.

2.2 Structure analysis

The powder constituent phase was determined with X-ray diffractometry (CuKa, Rigaku, Rint 2000) equipped with Cu Kα radiation ($\lambda = 1.5418$ Å). The morphology and microstructure were investigated with field emission scanning electron microscopy (FESEM, Hitachi S-4800). Transmission electron microscopy (TEM) investigations were carried out on a JEM 2010 microscope. Traditional standard TEM specimen preparation processes were used to prepare thin TEM specimens, consisting of cutting, grinding, mechanical polishing and low-voltage (1.5 V) Ar-ion milling on a liquid nitrogen cooling stage. The thin TEM specimens were nitrogen plasma cleaned for 30 s, and then used for scanning transmission electron microscopy (STEM) investigation (FEI Magellan 400) at an accelerating voltage of 30 kV. To evaluate the reduction degree of GO after the SPS process, X-ray photoelectron spectroscopy (XPS) was carried out on a pure GO compact treated by SPS under the same conditions as the SKD/GO samples. Both the as-prepared GO and the pure GO compact after SPS treatment were ion etched at 1 kV and 1 μA for 10 seconds on an area of 1 mm × 1 mm with an EX05 argon ion gun. The XPS analysis was conducted on a Thermo Scientific ESCALAB 250Xi with a monochromated Al X-ray source ($h\nu = 1486.6$ eV), operating at a beam energy of 15 kV, a beam current of 10 mA and an incident angle of 58°, while an electron flood gun was used for charge compensation.

2.3 Thermal property measurements

The SPS-sintered pellets were ground and polished into disk-shaped samples with 10 mm diameter and ~2 mm thickness for thermal diffusivity measurement. A thin graphite layer was coated on two sides of the disc samples to impede emissivity from the samples. The total thermal conductivity (κ) was calculated by $\kappa = \rho C_p \lambda$, where ρ is the density of the bulk samples determined by the Archimedes method (METTLER TOLEDO AB104-L), C_p is the specific heat determined by differential scanning calorimetry (DSC 404C, Netzsch, Germany). λ is the thermal diffusivity coefficient from 300 to 850 K measured on a Netzsch LFA427 by a laser flash method with an applied laser voltage of 450 V and a pulse width of 0.5 ms. The thermal diffusivity data were analyzed using a Cape–Lehman method with pulse correction.

2.4 Electrical property measurements

Rectangular bars with dimensions of ~8 mm × 2 mm × 2 mm were obtained by cutting in the radial direction of the SPS-sintered disc samples and subsequently used for the simultaneous measurement of electrical conductivity (σ) and Seebeck coefficient (S) from room temperature to 850 K under a helium atmosphere with a vacuum degree of −0.09 MPa on the ULVAC-RIKO ZEM-3 device. Rectangular bars with dimensions of ~5 mm × 2 mm × 1 mm were cut from the sintered pellet for low temperature electrical property characterization. A PPMS-Quantum Design was utilized to determine the electrical conductivity (σ) from 3 to 300 K with a four-probe configuration and Hall coefficient (R_H) with a five-probe configuration under a magnetic field of −5 T to 5 T. Measurements on both positive and negative magnetic field directions were carried out to minimize the magneto-resistance contributions as well as the voltage probe misalignment effects. The carrier concentration (n) was calculated from $R_H = 1/ne$, and the mobility (μ_H) from $\mu_H = \sigma/ne$, where e is the electron charge.

3. Results and discussion

3.1 Structure of the $Yb_{0.27}Co_4Sb_{12}$/rGO composite

Constructing a 3D-rGO network structure intercalated in a skutterudite matrix is the emphasis of this work. In order to evaluate the effectiveness of the SPS process in the reduction of GO, the pure GO compact was treated by SPS under the same conditions as sintering the SKD/GO compact and then X-ray photoelectron spectroscopy (XPS) analysis was conducted on the GO samples before and after SPS treatment. High resolution XPS spectra of C 1s are shown in Fig. 2a and b. The asymmetric C 1s peak can be fitted with peaks with binding energy at 284.6, 285.6, 286.9, and 288.6 eV, assigned to sp^2-C 1s, C–OH, C–O–C, and O=C–O bonds, respectively. It is clear that the peak of graphitic sp^2-C 1s at ~284.5 eV narrowed, while the signals of hydroxyl (C–O) ~285.6 eV and C–O–C ~286.9 eV became weaker and the peak of O=C–O at ~288.6 eV disappeared after SPS. All these observations deliver evidence that GO has been partially reduced by SPS treatment. It was reported that the reduction or partial deoxidization of oxides occurred during the SPS process under a vacuum in a graphite die due to the strong reducing atmosphere around the particles induced at high temperature[25–27] and the surface deoxidation effect[28,29] by electrical discharge. In the present experiment, graphene oxide is considered to be partially deoxidized by the accelerated thermal reduction in the SPS process.

The oxygen contents were also estimated from the XPS spectra and the O/C atomic ratio was determined. The O/C ratio decreased to a much lower value of 1/17.7 by SPS treatment from 1/2.2 for the as-prepared GO. Since most of the carbon atoms in GO are sp^3 hybridized, after chemical or thermal reduction, the size and numbers of sp^2 domains would increase and a percolated sp^2 network would grow on the basis of the

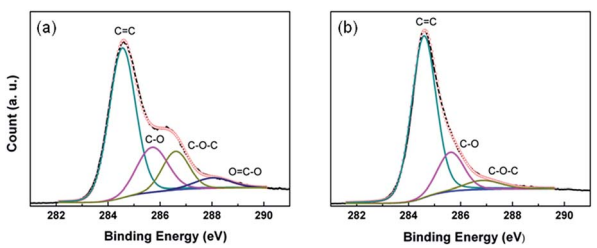

Fig. 2 Deconvoluted XPS spectra of (a) as-prepared GO and (b) rGO after SPS treatment.

sp^3-hybridized area, earmarking an insulator to semiconductor transition with decreased work function and band gap values.[30] The work function and band gap in rGO with different reduction degrees are reported to be dependent on the O/C ratio.[31,32] According to the theoretical relationship between the O/C ratio and work function proposed by Pritank *et al.*,[31] values of the work function are estimated to be ~5.3 for the as-prepared GO and ~4.7 eV for rGO after SPS, respectively. The values of band gap are estimated to be ~2.8 and ~0.5 eV for GO before SPS and rGO after SPS, respectively, according to Huang's relationship.[32] The reduction degree of the *in situ* sintered rGO under the same SPS conditions is regarded to be the same or similar. The dependence of composite performance on the reduction degree requires further study, for which new synthesis techniques should be developed.

Fig. 3a shows the typical TEM photograph of the GO-wrapped SKD particle obtained by the water solution suspending and filtering/drying process. GO has an ultrahigh specific surface energy,[19] and thus can readily wrap the suspending particles with excellent dispersion. Consequently, the SKD particles are well enclosed by ultrathin GO layers. The SEM photograph of the fractured surface of sintered SKD/rGO (0.72 vol%) (Fig. 3b) also shows that the rGO nano-layers are embedded on grain boundaries, as marked by the white arrows. A low-magnification TEM image (Fig. 3c) reveals that the matrix particles are distinctly and equably surrounded by rGO nano-layers as well. The high-magnification TEM image of the SKD/rGO (0.72 vol%) sample (Fig. 3d) further demonstrates that the particles are separated by rGO layers of ~3–5 nm, occasionally covering the phonon MFP of the filled skutterudite (~3 nm).[33,34]

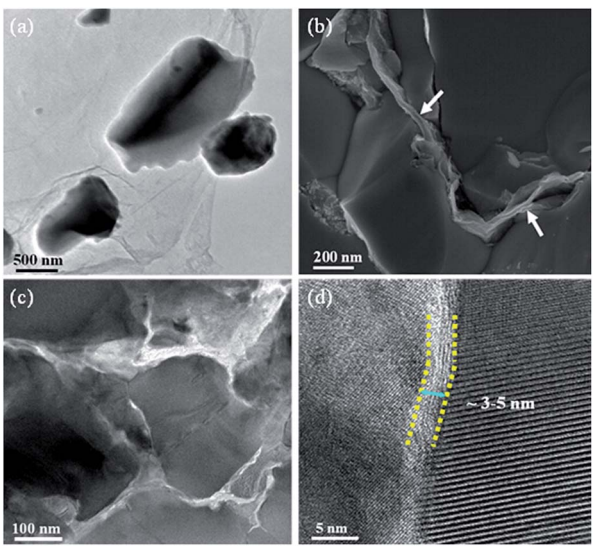

Fig. 3 Morphology and structure of the $Yb_yCo_4Sb_{12}$/rGO composite: (a) TEM image of GO-wrapped $Yb_{0.27}Co_4Sb_{12}$ obtained by solution dispersion and the filtering/drying process, (b) SEM image of the fractured surface of the sintered SKD/rGO surface showing rGO embedded on boundaries, (c) low-magnification TEM image showing the network wrapping architecture of rGO nanolayers and (d) high-magnification TEM image showing the rGO nanolayer of ~3–5 nm thickness for the 0.72 vol% 3D-rGO sample.

Comparatively, it is found that the average thickness of the rGO layers on the SKD grain boundary grows from ~3–5 nm for 0.72 vol% 3D-rGO to ~6–8 nm for the 1.8 vol% 3D-rGO sample, and ~10–12 nm for the 3.6 vol% 3D-rGO sample (see ESI, Fig. S2a and b†). The growing thickness may deteriorate electron transport and the detailed influence on the thermoelectric transport will be discussed later.

To make a visual display of the 3D-rGO network wrapping architecture, high angle annular dark-field imaging (HAADF) was conducted as shown in Fig. 4. The interconnected rGO constructs a network embedded on grain boundaries, which is bright white in Fig. 4. The EDS analysis in the inset reconfirms the existence of rGO on grain boundaries. From the above XPS analysis and TEM/SEM/STEM observation, it can be concluded that a 3D-rGO network wrapping architecture embedded in the SKD polycrystalline bulk is experimentally established through the *in situ* reduction approach.

3.2 Thermal transport of the $Yb_{0.27}Co_4Sb_{12}$/rGO composite

Fig. 5a shows the total thermal conductivity (κ) as a function of temperature for SKD/rGO samples with different rGO contents (y). The κ of the matrix sample ($Yb_{0.27}Co_4Sb_{12}$) is consistent with those of the $Yb_yCo_4Sb_{12}$ skutterudite reported previously.[14,16,38]

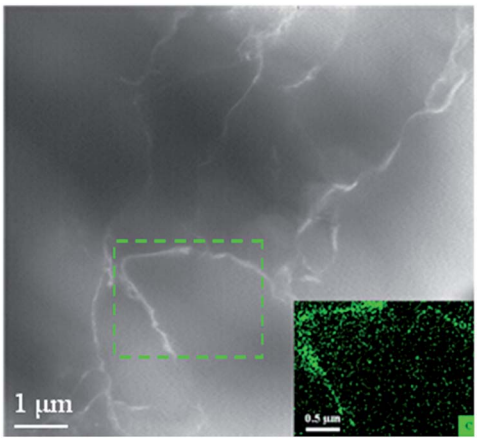

Fig. 4 HAADF-STEM image of the $Yb_{0.27}Co_4Sb_{12}$/1.8 vol% 3D-rGO wrapping sample. Inset: local energy spectrum analysis for carbon.

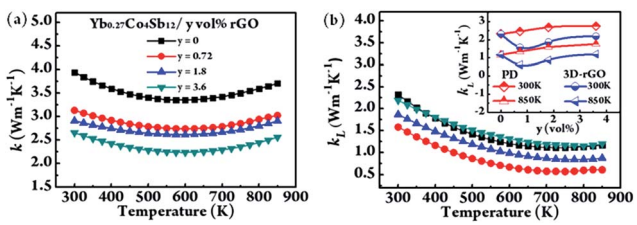

Fig. 5 (a) The thermal conductivity, and (b) lattice thermal conductivity as a function of temperature for $Yb_{0.27}Co_4Sb_{12}$/y vol% 3D-rGO (y = 0, 0.72, 1.8, 3.6) wrapping samples. Inset: rGO content (y) dependence of κ_L at 300 K, 850 K for 3D-rGO wrapping samples and particle dispersion (PD) samples obtained by direct mixing and the sintering process for comparison, respectively.

The κ values of the obtained 3D-rGO samples decrease significantly with increase of y, attributing to the decline of both κ_E (discussed later) and κ_L, where κ_L was computed by subtracting κ_E *via* the Wiedemann–Franz law from the total κ. Fig. 5b shows κ_L as a function of temperature for SKD/rGO samples. The κ_L of the 0.72 vol% 3D-rGO sample demonstrates the lowest value in the temperature range of 300–850 K. The lowest value of κ_L = 0.57 W m^{-1} K^{-1} (750 K), approaching the theoretical limit of the minimum value (0.3 W m^{-1} K^{-1}),[14] is considered to tremendously contribute to the depression of total thermal conductivity. The rGO content (y) dependency of κ and κ_L, typically at 300 and 850 K (inset in Fig. 5b) for 3D-rGO wrapping and PD (particle dispersion) samples, further proves the significance of κ_L depression especially at 0.72 vol%-rGO by the 3D-rGO wrapping structure. When the rGO content further increases, κ_L undergoes a gentle rise from 0.72 vol% to 3.6 vol%, and surpasses that of the matrix at 3.6 vol%. It is considered to be caused by the volume effect of the rGO dispersion phase, because the volume effect gradually becomes dominant compared to the interparticle and intraparticle boundary scattering effects when the content of the rGO dispersion phase (which possesses higher thermal conductivity) increases.[16] The HRTEM observation (see Fig. S2b†) indicated that the increasing rGO content leads to a thicker network layer of ~10–12 nm for the 3.6 vol% 3D-rGO sample.

3.3 Electrical transport of the $Yb_{0.27}Co_4Sb_{12}$/rGO composite

Fig. 6a shows the temperature-dependent electrical conductivity (σ) of the obtained 3D-rGO wrapping samples with different rGO contents (y). For the matrix SKD sample (0 vol%-rGO), σ values at room temperature and 850 K are 2.69 × 10^5 S m^{-1} and 1.49 × 10^5 S m^{-1}, respectively. The 0.72 vol% 3D-rGO sample shows almost the same values and same temperature dependence with the matrix SKD sample, *i.e.*, 2.58 × 10^5 S m^{-1} at room temperature and 1.42 × 10^5 S m^{-1} at 850 K. As illustrated in Fig. 3d, the 0.72 vol% 3D-rGO sample has an rGO network layer with a thickness of ~3–5 nm, which can strongly scatter phonons but have little influence on σ. rGO was reported to show p-type semiconduction above room temperature,[20,30] but a certain amount of the sp^2-conjuncted hexagonal graphene lattice is disrupted by C–O bonds which deteriorates the electron transport.[35] In the present case, when y is larger than 1.8 vol%, the thickness of the network layer soon becomes higher than 10 nm. As the thickness of the rGO layer increases, volume effects[16] for both thermal and electrical properties would gradually become dominant, leading to the deterioration of σ. The temperature dependence of σ undergoes a change from a degenerating semiconducting behavior to an intrinsic one ($d\sigma/dT$ changes from negative to positive). It remains a challenge to further characterize the electrical and thermal transport properties of the nano-rGO layers embedded on the matrix grain boundaries to reveal in depth the influence of the electrical and thermal transport properties of rGO on the composite performance.

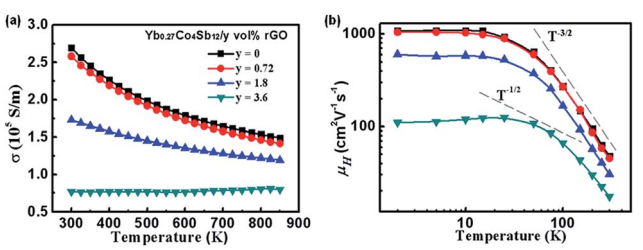

Fig. 6 (a) Electrical conductivity and (b) electron mobility as a function of temperature for $Yb_{0.27}Co_4Sb_{12}$/y vol% rGO (y = 0, 0.72, 1.8, and 3.6) 3D wrapping samples.

The electron transport properties of 3D-rGO wrapping samples are further investigated by the measurement of the electron mobility (μ_H), shown in Fig. 6b. For the 3D-rGO wrapping samples, when y = 0, the relationship of $\mu_H \propto T^\alpha$ ($\alpha = -3/2$) is observed near room temperature, manifesting a dominant mechanism of acoustic phonon scattering that agrees with reported data of pure filled skutterudites. The curves of 0.72 vol% and 1.8 vol% 3D-rGO samples resemble that of y = 0 ($\alpha = -3/2$), indicating that the same scattering mechanism dominates the transport in the samples with rGO content less than 1.8 vol%. However, for the 3.6 vol% sample, the scattering parameter was observed between −3/2 and −1/2 near room temperature, indicating that a mixed scattering mechanism dominates the transport in this sample.

Fig. 7 shows the Seebeck coefficients and power factors as a function of temperature and/or carrier concentration for the obtained 3D-rGO wrapping samples with different rGO contents (y). Electrons are the major carriers in $Yb_{0.27}Co_4Sb_{12}$/rGO samples showing negative S. All 3D-rGO wrapping samples have higher $|S|$ compared to that of the matrix. Owing to the Fermi level gap between the matrix and rGO, the band may bend away from the interface, whereby an extra potential at the boundaries thus would be produced. The energy barrier produced by the phase interface between the matrix and rGO would scatter electrons with low energy and enhance the S, called the energy-filtering effect.[36,37] Given a compound of a fixed band structure, the $|S|$ only depends on carrier density, and decreases with increasing n (carrier concentration). As shown in Fig. 7a, the $|S|$ values of all 3D-rGO wrapping samples increased with increasing rGO content, which does not only stem from the contribution of decreased carrier concentration. The Hall measurement indicates that the y = 0.72 sample (n = 3.42 × 10^{20} cm^{-3}, S = −127.1 μV K^{-1}) has almost the same n value but a higher $|S|$ compared to the y = 0 sample (n = 3.56 × 10^{20} cm^{-3}, S = −121.1 μV K^{-1}). Fig. 7b shows n-dependent S for $Yb_xCo_4Sb_{12}$,[38] nanoparticle-dispersed $Yb_xCo_4Sb_{12}$ (ref. 13 and 14) and $Yb_{0.27}Co_4Sb_{12}$/rGO (present work). All S values for $Yb_xCo_4Sb_{12}$ follow a linear curve of $|S|$ *vs.* n (logarithmic coordinate). However, the S values of some nanoparticle-dispersed systems ($Yb_yCo_4Sb_{12}$/GaSb) and the present samples deviate from the line, indicating a remarkably enhanced $|S|$ under a given carrier concentration. As it is proved, the energy-filtering effect is considered to depend on the phase-interface area between the 'host' and 'guest'.[39] The rGO network architecture provides an abundant phase-interface for energy filtering to enhance $|S|$. The enhancement of $|S|$ is comparable to Xiong's

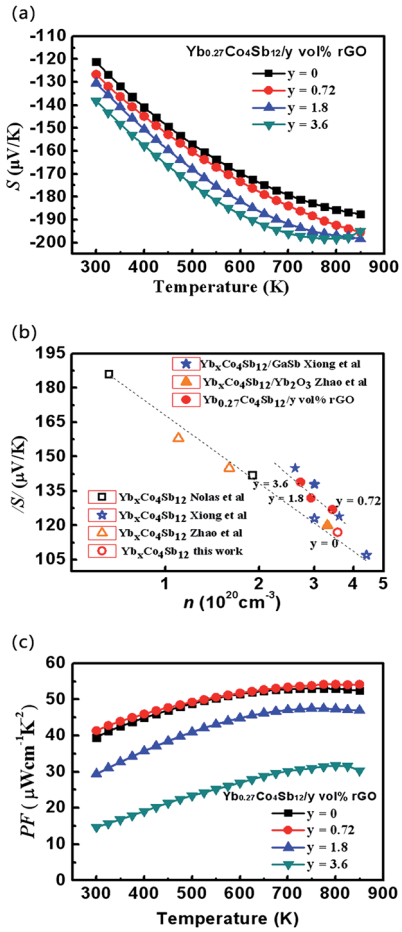

Fig. 7 (a) The Seebeck coefficient as a function of temperature, (b) carrier concentration dependent Seebeck coefficient in a logarithmic coordinate, and (c) power factor as a function of temperature for $Yb_{0.27}Co_4Sb_{12}/y$ vol% rGO (y = 0, 0.72, 1.8, and 3.6) 3D network wrapping samples.

$Yb_yCo_4Sb_{12}$/GaSb[16] composite. With a slight decrease of σ but enhanced $|S|$, the y = 0.72 sample exhibits slightly-improved power factors as shown in Fig. 7c. Especially, σS^2 of the y = 0.72 rGO sample reaches 41.4 μW cm^{-1} K^{-2} at room temperature and 54.2 μW cm^{-1} K^{-2} at 800 K, while σS^2 of the matrix is 39.4 μW cm^{-1} K^{-2} at room temperature and 52.4 μW cm^{-1} K^{-2} at 800 K, indicating that the increase of $|S|$ weighs over the decrease of σ.

3.4 Thermoelectric figure of merit

Temperature dependencies of ZT for all $Yb_{0.27}Co_4Sb_{12}$/rGO samples with 3D-rGO wrapping structure are shown in Fig. 8. The inset shows the y-dependence of ZT for comparison between 3D-rGO wrapping samples and particle-dispersed (PD) samples at 850 K. The ZT values of 3D-rGO wrapping samples show a remarkable enhancement when $y \leq 1.8$, then drop down with increase of y, and tend to merge with that of PD samples when $y \geq 3.6$. This result demonstrates that the 3D-rGO wrapping architecture can effectively depress thermal conductivity while maintaining or even raising electrical transport (power factor). Optimized ZT is achieved with a suitable rGO content ($y \leq 1.8$). But when the rGO content (y) increases to 3.6, the rGO layer becomes thick enough (see Fig. S2†) so that the volume effect begins to be dominant. The ZT value thus tends to resemble that of the y = 3.6 PD sample. If we define a $\Delta(ZT)/ZT$ as the ZT increase rate from the y = 0 sample (ZT_m) to y = 0.72, 1.8, and 3.6 samples (ZT_c), calculated by $\Delta(ZT)/ZT = (ZT_c - ZT_m)/ZT_m \times 100\%$, a prominent ZT increase rate of 32% (at 300 K), 26% (at 850 K) is achieved for the 0.72 vol% 3D-rGO sample. The ZT value reaches a peak of 1.51 at 850 K for the 0.72 vol% 3D-rGO sample. $\Delta(ZT)/ZT$ of the 1.8 vol% 3D-rGO sample is relatively low, but positive and increases up to 11% (ZT = 1.34, at 850 K). Considering the whole temperature range from 300–850 K, the average ZT value ZT_{ave} of the 0.72 vol% 3D-rGO sample reached 1.13. We can expect an optimal thermoelectric conversion efficiency η_{opt} (ref. 40) of 16.3%, outclassing the results of single filled skutterudite and their composites previously reported.

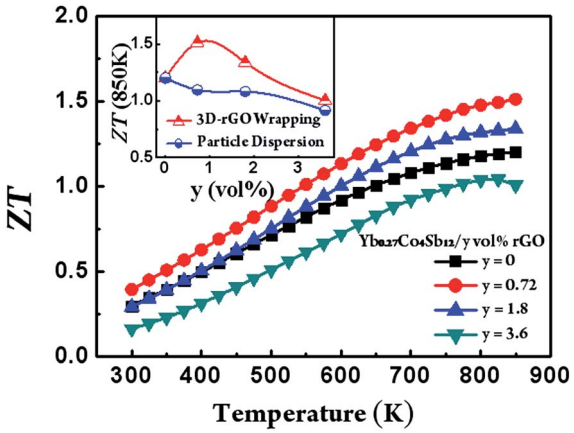

Fig. 8 Temperature-dependent ZT for $Yb_{0.27}Co_4Sb_{12}/y$ vol% rGO (y = 0, 0.72, 1.8, and 3.6) 3D wrapping samples from 300–850 K. Inset: comparison of y-dependent ZT between 3D-rGO wrapping samples and particle dispersion samples at 850 K.

4. Conclusions

$Yb_yCo_4Sb_{12}$-based composites with rGO intercalated on the $Yb_yCo_4Sb_{12}$ grain boundary forming a 3D network wrapping architecture have been synthesized by an *in situ* reduction process. When the rGO content is less than 1.8 vol%, the thickness of the rGO layer on the grain boundary of the $Yb_yCo_4Sb_{12}$ matrix is less than 10 nm, and the lattice thermal conductivity is greatly decreased while the power factor maintains a slight change resulting in a great enhancement in ZT. The 3D-rGO network-wrapping architecture using GO as the precursor goes beyond the nanoparticle dispersion system and takes advantage of phonon constraints of wider wavelengths. A giant depression of κ_L by ~34–58% and then a ZT value up to 1.51 at 850 K are achieved. This result outperforms all reported single-filled skutterudites and their nano-composites, which earmarks the 3D-rGO network wrapping architecture to be a competitive route to state-of-the-art thermoelectric materials.

Acknowledgements

This work was supported by the National Natural Science Foundation of China (no. 51121064 and no. 11179013) and 973 Program of National Basic Research Program of China (no. 2013CB632501). Y. Zhu appreciates the support from the Natural Science Foundation of China (no. 51322204) and the Fundamental Research Funds for the Central Universities (no. WK2060140014). P. Zong also thanks Dr Lin Tianquan for kind help in XPS spectra analysis.

Notes and references

1 K. Biswas, J. Q. He, I. D. Blum, C. I. Wu, T. P. Hogan, D. N. Seidman, V. P. Dravid and M. G. Kanatzidis, *Nature*, 2012, **489**, 414.
2 G. J. Snyder and E. S. Toberer, *Nat. Mater.*, 2008, **7**, 105.
3 X. Shi, J. Yang, R. J. Salvador, M. F. Chi, Y. J. Cho, H. Wang, S. Q. Bai, J. H. Yang, W. Q. Zhang and L. D. Chen, *J. Am. Chem. Soc.*, 2011, **133**, 7837.
4 Y. Z. Pei, X. Y. Shi, A. Lalonde, H. Wang, L. D. Chen and G. J. Snyder, *Nature*, 2011, **473**, 66.
5 H. L. Liu, X. Shi, F. F. Xu, L. L. Zhang, W. Q. Zhang, L. D. Chen, Q. Li, C. Uher, T. Day and G. J. Snyder, *Nat. Mater.*, 2012, **11**, 422.
6 L. D. Zhao, S. Q. Hao, S. H. Lo, C. I. Wu, X. Y. Zhou, Y. Lee, H. Li, K. Biswas, T. P. Hogan, C. Uher, C. Wolverton, V. P. Dravid and M. G. Kanatzidis, *J. Am. Chem. Soc.*, 2013, **135**, 7364.
7 Y. L. Pei, H. J. Wu, D. Wu, F. S. Zheng and J. Q. He, *J. Am. Chem. Soc.*, 2014, **136**, 13902.
8 L. D. Zhao, S. H. Lo, Y. Zhang, H. Sun, G. Tan, C. Uher, C. Wolverton, V. P. Dravid and M. G. Kanatzidis, *Nature*, 2014, **508**, 373.
9 R. J. Korkosz, T. C. Chasapis, S. Lo, J. W. Doak, Y. J. Kim, C. I. Wu, E. Hatzikraniotis, T. P. Hogan, D. N. Seidman, C. Wolverton, V. P. Dravid and M. G. Kanatzidis, *J. Am. Chem. Soc.*, 2014, **136**, 3225.
10 L. D. Zhao, H. J. Wu, S. Q. Hao, C. I. Wu, X. Y. Zhou, K. Biswas, J. Q. He, T. P. Hogan, C. Uher, C. Wolverton, V. P. Dravid and M. G. Kanatzidis, *Energy Environ. Sci.*, 2013, **6**, 3346.
11 X. Shi, L. D. Chen, J. Yang and G. P. Meisner, *Appl. Phys. Lett.*, 2004, **84**, 2301.
12 Z. He, C. Stiewe, D. Platzek, G. Karpinski, E. Müller, S. H. Li, M. Toprak and M. Muhammed, *J. Appl. Phys.*, 2007, **101**, 043707.
13 Z. Xiong, X. H. Chen, X. Y. Zhao, S. Q. Bai, X. Y. Huang and L. D. Chen, *Solid State Sci.*, 2009, **11**, 1612.
14 X. Y. Zhao, X. Shi, L. D. Chen, W. Zhang, S. Q. Bai, Y. Z. Pei, X. Y. Li and T. Goto, *Appl. Phys. Lett.*, 2006, **89**, 092121.
15 H. Li, X. Tang, X. Su and Q. Zhang, *Appl. Phys. Lett.*, 2008, **92**, 202114.
16 Z. Xiong, X. H. Chen, X. Y. Huang, S. Q. Bai and L. D. Chen, *Acta Mater.*, 2010, **58**, 3995.
17 S. J. Poon, A. S. Petersen and D. Wu, *Appl. Phys. Lett.*, 2013, **102**, 173110.
18 L. D. Chen, Z. Xiong and S. Q. Bai, *J. Inorg. Mater.*, 2010, **25**, 561.
19 Y. W. Zhu, S. Murali, W. Cai, X. Li, J. W. Suk and J. Potts, *Adv. Mater.*, 2010, **22**, 3906.
20 N. Xiao, X. C. Dong, L. Song, D. Y. Liu, Y. Y. Tay, X. S. Wu, L. J. Li, Y. Zhao, T. Yu, H. Zhang, W. Huang, H. H. Hng, P. M. Ajayan and Q. Y. Yan, *ACS Nano*, 2011, **5**, 2749.
21 S. Stankovich, R. D. Piner, X. Q. Chen, N. Q. Wu, S. T. Nguyen and R. S. Ruoff, *J. Mater. Chem.*, 2006, **16**, 155.
22 B. Feng, J. Xie, G. S. Cao, T. J. Zhu and X. B. Zhao, *J. Mater. Chem. A*, 2013, **1**, 13111.
23 J. D. Dong, W. Liu, H. Li, X. L. Su, X. F. Tang and C. Uher, *J. Mater. Chem. A*, 2013, **1**, 12503.
24 W. S. Hummers and R. E. Offeman, *J. Am. Chem. Soc.*, 1958, **80**, 1339.
25 S. Ran, J. Vleugels, S. Huang, K. Vanmeensel, D. H. A. Blank and L. Winnubst, *J. Eur. Ceram. Soc.*, 2010, **30**, 899.
26 S. Yoon, J. Dornseiffer, Y. Xiong, D. Grüner, Z. Shen, S. Iwaya, C. Pithan and R. Waser, *J. Eur. Ceram. Soc.*, 2011, **31**, 773.
27 N. Mahmed, O. Heczko, R. Maki, O. Söderberg, E. Haimi and S. Hannula, *J. Eur. Ceram. Soc.*, 2012, **32**, 2981.
28 N. Toyofuku, T. Kuramoto, T. Imai, M. Ohyanagi and Z. A. Munir, *J. Mater. Sci.*, 2012, **47**, 2201.
29 X. P. Li, M. Yan, H. Imai, K. Kondoh, G. B. Schaffer and M. Qian, *J. Non-Cryst. Solids*, 2013, **375**, 95.
30 C. Punckt, F. Muckel, S. Wolff, I. A. Aksay, C. A. Chavarin, G. Bacher and W. Mertin, *Appl. Phys. Lett.*, 2013, **102**, 023114.
31 V. K. Pritank, B. Marco and C. G. Jefferey, *ACS Nano*, 2013, **7**, 1642.
32 H. M. Huang, Z. B. Li, J. C. She and W. L. Wang, *J. Appl. Phys.*, 2012, **111**, 054317.
33 T. Caillat, A. Borshchevsky and J. P. Fleurial, *J. Appl. Phys.*, 1996, **80**, 4442.
34 J. Yang, W. Zhang, S. Q. Bai, Z. Mei and L. D. Chen, *Appl. Phys. Lett.*, 2007, **90**, 192111.
35 D. H. Sim, Q. Yan, D. Liu, X. Dong, N. Xiao, S. Li, Y. Zhao, L. J. Li, Q. Y. Yan and H. H. Hng, *J. Phys. Chem. C*, 2011, **115**, 1780.
36 J. P. Heremans, V. Jovovic, E. S. Toberer, A. Saramat, K. Kurosaki, A. Charoenphakdee, S. Yamanaka and G. J. Snyder, *Science*, 2008, **321**, 554.
37 S. V. Faleev and F. Léonard, *Phys. Rev. B: Condens. Matter Mater. Phys.*, 2008, **77**, 214304.
38 G. S. Nolas, M. Kaeser, I. R. Littleton and T. M. Tritt, *Appl. Phys. Lett.*, 2000, **77**, 1855.
39 S. Katsuyama, M. Watanabe, M. Kuroki, T. Maehata and M. Ito, *J. Appl. Phys.*, 2003, **93**, 2758.
40 B. Poudel, Q. Hao, Y. Ma, Y. C. Lan, A. Mininnich, B. Yu, X. Yan, D. Z. Wang, A. Muto, D. Vashaee, X. Y. Chen, J. M. Liu, M. Dresselhaus, G. Chen and Z. F. Ren, *Science*, 2008, **320**, 634.